



Star Proper Motions Based on Two-epoch Observations from the SDSS and DESI Imaging Surveys

YUN-AO XIAO ^{1,2} HU ZOU ^{1,2} XIN XU,³ LU FENG,¹ WEI-JIAN GUO,¹ WEN-XIONG LI,¹ ZHI-XIA SHEN,¹ GAURAV SINGH,¹
JI-PENG SUI,^{1,2} JIA-LI WANG,¹ AND SUI-JIAN XUE¹

¹Key Laboratory of Optical Astronomy, National Astronomical Observatories, Chinese Academy of Sciences, Beijing 100101, P.R. China

²University of Chinese Academy of Sciences, Beijing 100039, P.R. China

³Kapteyn Astronomical Institute, University of Groningen, PO BOX 800, 9700 AV Groningen, The Netherlands

ABSTRACT

In this study, we present the construction of a new proper motion catalog utilizing the photometric data from the Sloan Digital Sky Survey (SDSS) and Dark Energy Spectroscopic Instrument (DESI) imaging surveys, with a median time baseline of about 13 years. To mitigate systematic errors, the DESI galaxy positions are employed to establish a reference frame and to correct the position-, magnitude-, and color-dependent discrepancies between SDSS and DESI imaging datasets. Spanning 12,589 square degrees, the catalog encompasses about 206.6 million non-Gaia objects down to $m_r \sim 23$. Based on 734k quasars, the assessment of the global systematic errors in DESI-SDSS proper motion catalog yields values of 0.14 mas yr^{-1} for μ_{α^*} and 0.11 mas yr^{-1} for μ_δ . The catalog exhibits a precision surpassing 3.7 mas yr^{-1} , albeit varying with position, color, and magnitude. An additional evaluation employing approximately 5,300 distant star samples yields an overall precision of approximately 3.0 and 2.9 mas yr^{-1} for μ_{α^*} and μ_δ , respectively. Further comparisons with proper motions from SDSS Stripe 82 reveal a strong consistency between the two datasets. As a practical application, we utilize fainter non-Gaia objects in our catalog to update the proper motions of 17 star clusters. The resulting proper motions for these clusters exhibit excellent consistency with those derived from Gaia data. Our proper motion measurements, characterized by a deeper limiting magnitude, stands as a valuable complement to the Gaia dataset. The catalog is publicly available at <https://www.scidb.cn/s/YzaIv2>.

Keywords: Astrometry – Astronomical databases: miscellaneous – Proper Motions

1. INTRODUCTION

The vast repository of knowledge derived from the Milky Way is a cornerstone of modern astrophysics. For over a century, the scientific community has dedicated substantial effort to elucidating the intricate structure and dynamic behavior of the Milky Way (Helmi 2020; Cooper et al. 2023). Central to this pursuit is the six-dimensional phase space information, encompassing both the positions and velocities of various galactic constituents, such as stars, clusters, tidal streams, and satellites (Katz et al. 2018; Malhan et al. 2018; Cantat-Gaudin 2022; Drimmel et al. 2023). Proper motion provides a tangential component of the three-dimensional velocity vector, which is the observed position change of a celestial object over time relative to the background sources. It is crucial for illuminating the assembly history and dynamic evolution of our Galaxy.

The measurement of proper motion involves the comparative analysis of celestial coordinates for stars captured at different epochs. Early proper motion catalogs were established primarily through the use of multiple exposures from

the same survey over varying time periods. These surveys either spanned nearly the entire sky with relatively shallow observations (e.g. Hog et al. 2000; Zacharias et al. 2000; Monet et al. 2003) or targeted smaller yet more intensively scrutinized regions of the sky (e.g. Hambly et al. 2001; Munn et al. 2004). The advent of both wide-field and highly sensitive photometric surveys subsequently enabled us to determine star proper motions more precisely using long-time baselines between different surveys (e.g. Qiu et al. 2021; Tian et al. 2017; Peng et al. 2015).

Measurement of proper motion necessitates the determination of a star motion relative to a well-defined velocity reference frame. Broadly speaking, there exist two fundamental strategies to align proper motions with an inertial frame, as outlined by (Tian et al. 2017). The first approach involves leveraging a high-precision catalog already firmly anchored to the International Celestial Reference System (ICRS) and subsequently incorporating faint sources into this frame. Such catalogs are exemplified by Tycho-2 (Hog et al. 2000), PP-MXL (Roesser et al. 2010), and UCAC4 (Zacharias et al. 2013). Alternatively, one may construct a reference frame by harnessing distant celestial objects whose proper motions are negligible, such as galaxies and quasars. This methodology entails meticulous cross-calibration of observations obtained

at different epochs. The SDSS proper motion catalog (Munn et al. 2004) and the XPM catalog (Fedorov et al. 2009) were assembled following this approach.

Employing the South Galactic Cap U -band Sky Survey (SCUSS; Zou et al. 2016), Peng et al. (2015) determined absolute proper motions for some 7.7 million celestial bodies via astrometric comparison with the Sloan Digital Sky Survey (SDSS; York et al. 2000). They implemented the APOP technique (Qi et al. 2015) to construct a reference frame utilizing background galaxies, thereby mitigating systematic errors associated with position, magnitude, and color. The SCUSS proper motion catalog records systematic errors of 0.08 mas yr^{-1} and 0.06 mas yr^{-1} for respective components. Tian et al. (2017) computed stellar proper motions using data from Gaia DR1 (Gaia Collaboration et al. 2016; Lindegren et al. 2016), Pan-STARRS1 (PS1; Chambers et al. 2016), SDSS, and 2MASS (Skrutskie et al. 2006). They established a reference frame based on galaxy positions within PS1 and derived proper motions by examining star positions across up to nine distinct epochs in those surveys. GPS1 contains the proper motions of 350 million sources down to $m_r \sim 20$ and exhibits small systematic errors ($<0.3 \text{ mas yr}^{-1}$) and high precision ($\sim 1.5 \text{ mas yr}^{-1}$).

The trailblazing Gaia mission unveiled its third dataset in 2023 (Gaia Collaboration et al. 2023), exponentially boosting the count of celestial objects with precisely determined proper motions to an impressive 1.5 billion. Among stars brighter than 20.8 mag, a remarkable 97% exhibit typical uncertainties in proper motion better than 1.5 mas yr^{-1} . Nonetheless, current Gaia proper motion measurements remain constrained by their limiting magnitudes. Wide and deep photometric surveys hold the potential to compile proper motion catalogs reaching deeper into the realm of faint stars, thereby facilitating investigations of the farthest extents and the kinematics of more distant populations in our Galaxy. The legacy imaging surveys of the Dark Energy Spectroscopic Instrument (DESI; Dey et al. 2019) deliver optical imaging data with 2–3 magnitudes deeper than SDSS (Fukugita et al. 1996; Hogg et al. 2001). Spanning nearly the entire SDSS sky coverage, these surveys present a substantial temporal baseline of approximately a decade. In this paper, we capitalize on these rich resources by merging the two photometric datasets to yield a proper motion catalog encompassing stars dimmer than the magnitude limit imposed by Gaia.

The structure of this paper is outlined as follows. Section 2 describes the SDSS and DESI imaging data utilized in the derivation of the proper motion catalog. Section 3 elucidates the methodology employed for the catalog construction. Section 4 presents the systematic errors and precision of the derived proper motions as gauged through diverse celestial objects, encompassing galaxies, quasars, and distant halo stars, and comparisons with other established proper motion catalogs. Section 5 discusses the limitations inherent in our catalog and provides an application example for the determination of proper motions in star clusters situated within the catalog sky coverage. Section 6 gives the summary. Throughout this paper, we adopt the notation α and δ to represent the

right ascension and declination, respectively. Furthermore, we employ α_* to signify the right ascension in the gnomonic projection coordinate system, such as $\mu_{\alpha_*} = \mu_{\alpha} \cos(\delta)$, and $\sigma_{\alpha_*} = \sigma_{\alpha} \cos(\delta)$. In addition, all the magnitudes are in AB mag and corrected for the Galactic extinction using the dust map of Schlegel et al. (1998).

2. DATA

2.1. SDSS survey data

The SDSS is one of the most successful and influential projects, characterized by both photometric and spectroscopic surveys, using a 2.5-meter telescope. This telescope is instrumented by a wide-area, multiband CCD camera and multi-object fiber-fed spectrographs (Gunn et al. 2006). The SDSS survey covers roughly one third of the celestial sphere. It has performed concurrent observations across five photometric bands of u , g , r , i , and z , with a broad wavelength coverage ranging from 3000 to 11,000 Å. The 5σ limiting magnitudes for these bands are respectively 22.1, 23.2, 23.1, 22.5, and 20.8 mag. The saturation magnitudes are approximately 13.5, 15.0, 15.5, 15.0, and 14.0 mag in u , g , r , i , and z bands, respectively (Gunn et al. 1998). The typical astrometric uncertainties for brighter stars with $r < 19.0$ are in the range of 20 to 30 mas (Stoughton et al. 2002).

Since commencing regular operations in 2000, the SDSS has progressed through multiple stages. During SDSS-I (2000–2005), the primary objective was to conduct a “Legacy” survey encompassing five-band imaging and spectroscopy of well-targeted galaxy and QSO samples (York et al. 2000). Following this, SDSS-II (2005–2008) completed the Legacy survey and further explored the three-dimensional clustering of one million galaxies and 100,000 quasars (Abazajian et al. 2009). Subsequently, SDSS-III, IV, and V (2008–present) have predominantly concentrated on spectroscopic observations. SDSS-III expanded the imaging coverage by adding an extra 2395 deg² in the Southern Galactic Cap (SGC), bringing the cumulative imaging area to approximately 14,500 deg² (Aihara et al. 2011). In our study, we specifically utilized the photometric data from SDSS Data Release 12 to calculate the proper motion.

2.2. DESI Legacy Imaging Surveys

The DESI is designed to undertake a large-scale spectroscopic redshift survey using the 4-meter Mayall telescope. It is capable of simultaneously observing 5,000 celestial objects and plans to obtain about 40 million spectra. The main goal is to explore the structure growth and expansion history of the universe (DESI Collaboration et al. 2016).

The DESI legacy imaging surveys (hereafter LS) serve as the source for spectroscopic targets in the DESI project (Dey et al. 2019). These surveys unite three publicly accessible optical survey programs, including the Beijing-Arizona Sky Survey (2015–2019) (BASS; Zou et al. 2017), the Mayall z -band Legacy Survey (2016–2018) (MzLS; Silva et al. 2016), and the Dark Energy Camera Legacy Survey (2014–2019) (DECaLS; Blum et al. 2016). In this study, we utilize the Data Release 9 released in 2021, which also incorporates

imaging data from the Dark Energy Survey (DES; [Dark Energy Survey Collaboration et al. 2016](#)). The survey footprint spans a total sky coverage of approximately 20,000 square degrees. The imaging data from this release present 5σ limiting magnitudes of 24, 23.5, and 22.9 mag for g , r , and z bands, respectively. Moreover, the astrometry associated with these surveys is tied to Gaia Data Release 2 ([Gaia Collaboration et al. 2018](#)). Typically, for stars with $r > 21.0$, the astrometric uncertainties are less than 30 mas.

The temporal difference between SDSS and DESI observation epochs is calculated. Figure 1 shows the histogram of the time interval. This time interval varies broadly from a minimum of 5 years to a maximum of 19 years, with a median value of about 13 years. Such a lengthy time baseline significantly contributes to reducing inherent errors in proper motion estimation. There are two peaks in the time interval distribution, which correspond to early observations by SDSS-I & II and more recent observations in the SGC by SDSS-III, respectively. This difference in time intervals caused by SDSS observations can be clearly seen in Figure 2. In particular, the SDSS positions employed here are derived from single exposures. In contrast, each of the three DESI bands captures three observations, with the positional and temporal data utilized here representing the averaged values across these observations.

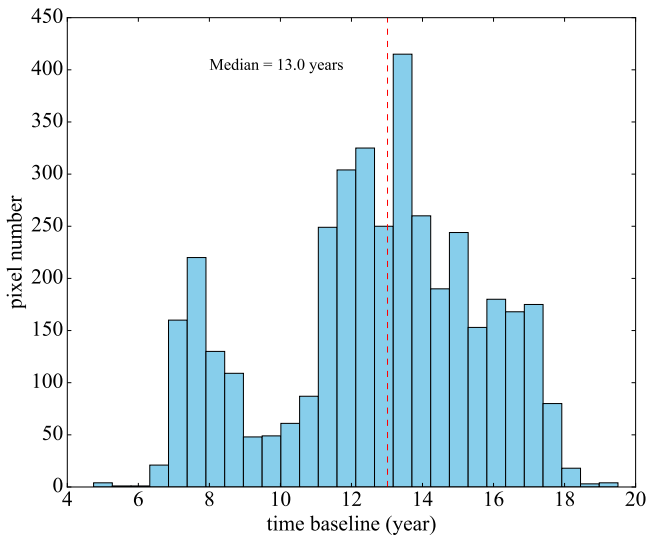


Figure 1: Distribution of the time intervals for celestial sources between the SDSS and DESI observations. The red dashed line represents the median value.

3. CONSTRUCTING THE DESI-SDSS PROPER MOTION CATALOG

Ideally, point sources are advantageous for establishing a reference frame due to their narrow Full Width at Half Maximum (FWHM), which enhances the positional measurement precision ([Fritz et al. 2010](#)). Nonetheless, the dearth of extragalactic point sources poses a challenge for constructing

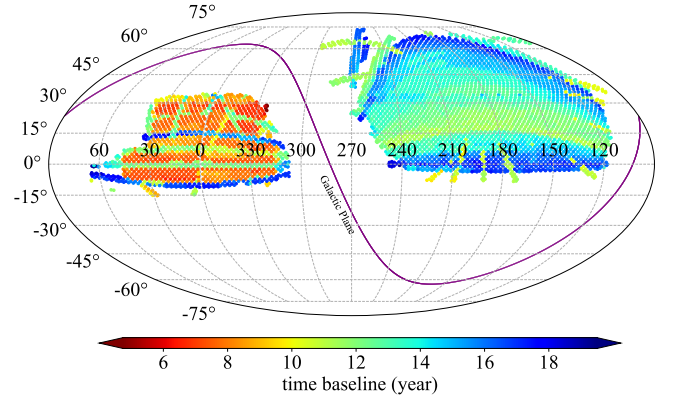


Figure 2: Spatial distribution of the time interval between SDSS and DESI observations. The purple curve represents the Galactic plane.

such a framework. Quasars, despite being candidates, are too sparsely distributed. Alternatively, Milky Way stars with accurately measured velocities could serve this purpose, such as those stars in the *Hipparcos* catalog ([Hog et al. 2000](#)). Unfortunately, these stars are too bright so that most of them are saturated in both SDSS and DESI observations, rendering them unsuitable for our purposes. Consequently, this work adopts galaxies as the foundation for the reference frame. The abundance of galaxies can considerably mitigate systematic errors, enhancing the accuracy of our analyses.

The procedure is outlined as follows. First, we cross-match the SDSS and DESI catalogs utilizing a $1''$ matching radius, yielding a shared sky coverage of $12,589 \text{ deg}^2$, which contains approximately 260 million objects. Taking into account the unique DESI photometric strategy that employs Gaia coordinates directly for photometry, we exclude these Gaia-detected objects (around 52.6 million) from subsequent analysis. Subsequently, position-, magnitude-, and color-dependent corrections are made to eliminate any systematic differences between the two surveys. Ultimately, the corrected coordinate displacements between DESI and SDSS observations yield the final proper motion calculations.

3.1. Correction for Position-dependent Astrometric Offsets

Prior to proper motion computation, the selection of background galaxy samples is imperative, alongside establishing a reference frame anchored on DESI-derived coordinates for these chosen galaxies. Following this, corrections are applied to address the systematic positional discrepancies of galaxies present in the SDSS catalog. It aims to align them with the established reference frame. These positional offsets, influenced by atmospheric and instrumental conditions, exhibit regional variability across the sky.

To account for the spatially varying offset, the merged DESI-SDSS dataset is segmented into equal-area pixels using HEALPix ([Gorski et al. 2005](#)). Each pixel has a sky area of 0.21 deg^2 (approximately $0.46^\circ \times 0.46^\circ$). While [Tian et al. \(2017\)](#) reported minimal variation in positional offsets and root mean square values when transitioning between $1^\circ \times 1^\circ$

and $0.5^\circ \times 0.5^\circ$ pixel sizes, our trials with both sizes uncover reduced errors in the final proper motion computations with smaller pixel size. Nevertheless, shrinking pixel dimensions further risks undermining the statistical validity due to insufficient galaxy numbers per pixel. Hence, the pixel size of 0.21 deg^2 ($n_{\text{side}} = 128$ in HEALPix) is adopted to achieve an optimal balance between precision and statistical robustness.

In the process of identifying the reference galaxy sample, we impose the following criteria for selection:

- (1) $16 < \text{MAG_R} < 21.5$ (magnitude cut),
- (2) $\text{MAGERR_R} < 0.15$ (magnitude error cut),
- (3) $\text{TYPE_SDSS} = 3$ & $\text{TYPE_DESI} \neq \text{PSF}$ (morphological classification as galaxy in both surveys);
- (4) $\text{GAIA_PHOT_G_MEAN_MAG} = 0$ (non-Gaia objects),

where MAG_R is the r -band magnitude measured by DESI, MAGERR_R is its associated error, TYPE_SDSS and TYPE_DESI are denoted classification parameters provided respectively by SDSS and DESI, and $\text{GAIA_PHOT_G_MEAN_MAG}$ is the Gaia G -band magnitude. Applying these filters enables the isolation of non-Gaia galaxies exhibiting relatively small positional measurement uncertainties from DESI. The left panel of Figure 3 shows the histogram of the galaxy numbers for all pixels. The median value is around 1100, a density that effectively curtails the position error of the reference frame to under 5 mas, prior to accounting for the time baseline.

The right panel of Figure 3 presents the spatial distribution of the galaxy numbers for all pixels. In pixels hosting over 800 galaxy samples, we compute the 3σ median of the positional discrepancies ($\Delta\alpha_*$ and $\Delta\delta$) between SDSS and DESI coordinates. Nevertheless, pixels situated along the periphery of the survey footprint often contain fewer than 800 galaxies. To uphold the high precision of the reference frame, we implement a tailored approach for these marginal pixels. Initially, we pinpoint the neighboring pixel with the largest galaxy population within a 1° radius. If no pixel hosts more than 800 galaxies, our searching radius expands to 2° . In instances where even this wider radius fails to yield a pixel with a sufficient galaxy count, we consolidate all galaxy samples from the surrounding pixels within this 2° boundary to calculate the astrometric offset.

The upper panels of Figure 4 illustrate the median positional offsets between the SDSS and DESI observations, while the lower panels present the error of the median offset, which is calculated as the standard deviation of the offsets divided by the square root of the galaxy number. A notable characteristic is that the majority of pixels exhibit an offset below 5 mas. Nonetheless, minor-scale fluctuations, on the order of ± 100 mas, are visible in the median offset patterns. We apply corrections to the SDSS source coordinates by adjusting them according to the computed median offsets in both α_* and δ .

3.2. Corrections for color- and magnitude-dependent astrometric offsets

Despite the positional corrections previously detailed, a residual discrepancy persists between the corrected SDSS source positions and the established reference frame. This lingering discrepancy exhibits a dependency on both the magnitude and color of sources, necessitating additional correction measurements. Its origin lies in multifaceted factors, such as atmospheric refraction, imprecise measurements for faint objects, and the differential chromatic refraction (DCR) effect (Kaczmarczik et al. 2009). Atmospheric refraction, a result of the Earth’s atmosphere bending incoming light, displaces celestial sources towards the zenith. This displacement angle is influenced by atmospheric conditions and is dependent on the wavelength. The DCR-induced blurring of the point spread function (PSF) in imaging observations affects the position measurement accuracy. Given that both SDSS and DESI surveys are conducted by ground-based telescopes, the astrometry is susceptible to the DCR effect. To correct for those magnitude- and color-dependent astrometric offsets, we draw more galaxies from a broader area.

We commence by addressing the positional offset attributable to color variations. In each pixel, a reference galaxy sample is collated from contiguous pixels within a radius of 2.5° or 5° . Here, we adopt the wider radius when the galaxy count within 2.5° falls short of 2,000. The selection criteria for the reference galaxy samples are similar to those in the process of the position-dependent correction, except enforcing a stricter magnitude error threshold ($\text{MAGERR_R} < 0.1$) to enhance the accuracy of color determinations. Galaxies are then segregated into multiple color bins. The upper panels of Figure 5 show the positional offset in δ as functions of color and magnitude at different declinations. For color bins central to the figure (where $1.0 < g - z < 2.5$) of this figure, given the ample quantity of galaxies, they have been evenly distributed with an interval of 0.25. Conversely, at both magnitude ends, the bin sizes increment to ensure a minimum count of 200 galaxies per bin. Inside these bins, we compute the 3σ median (μ) positional offset and the standard error (σ). Further, a third-degree polynomial fit, inversely weighted by σ , is applied to μ as a function of the color $g - z$. From Figure 5, we can see that the color-related corrections exhibit a clear variation across different declinations. This confirms that we need to make color corrections in different sky positions. The resulting fits for the offsets in α_* and δ are used to correct the SDSS source coordinates.

The correction procedure for magnitude-induced offsets is similar to that of the above color-induced correction. But we impose a different magnitude limit of $15 < \text{MAG_R} < 23$ and implement a fifth-order polynomial fitting. The lower panels of Figure 5 demonstrate the magnitude-dependent corrections. Except for the brightest and faintest ends, the overall correction is less than ~ 1 mas. Through all of the aforementioned corrections, the coordinates of all SDSS sources have been realigned to coincide with the DESI reference frame. The ultimate proper motion is calculated as the displacement between the DESI coordinate and corrected SDSS position, divided by the total span of time elapsed between the obser-

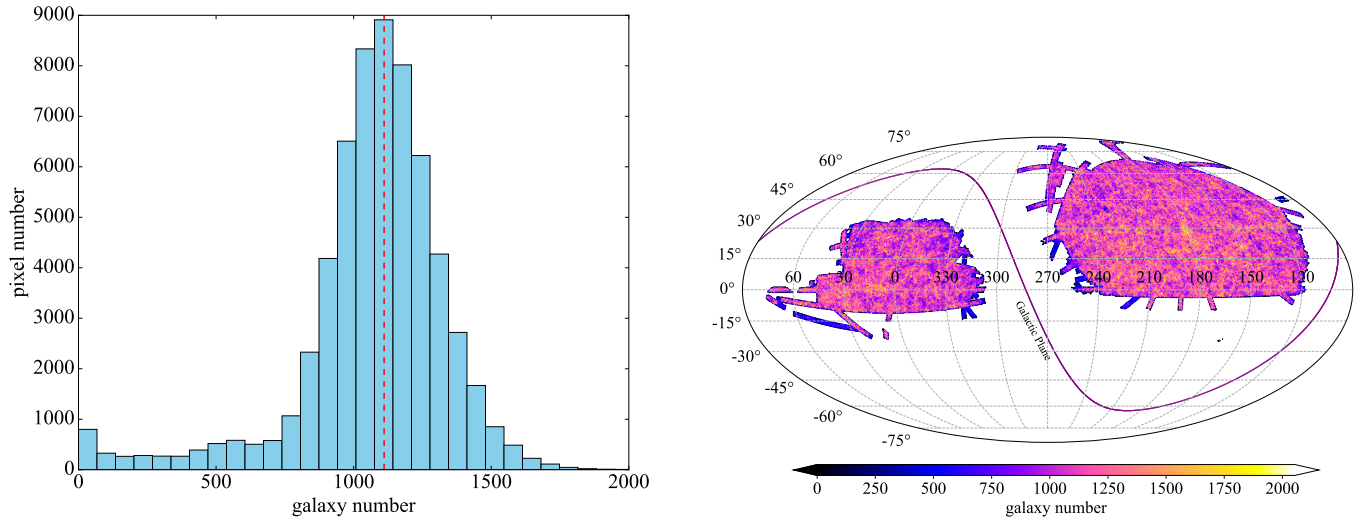


Figure 3: Left: histogram of galaxy numbers for all pixels. The dashed line shows the median value. Right: spatial distribution of galaxy numbers. The purple curve represents the Galactic plane.

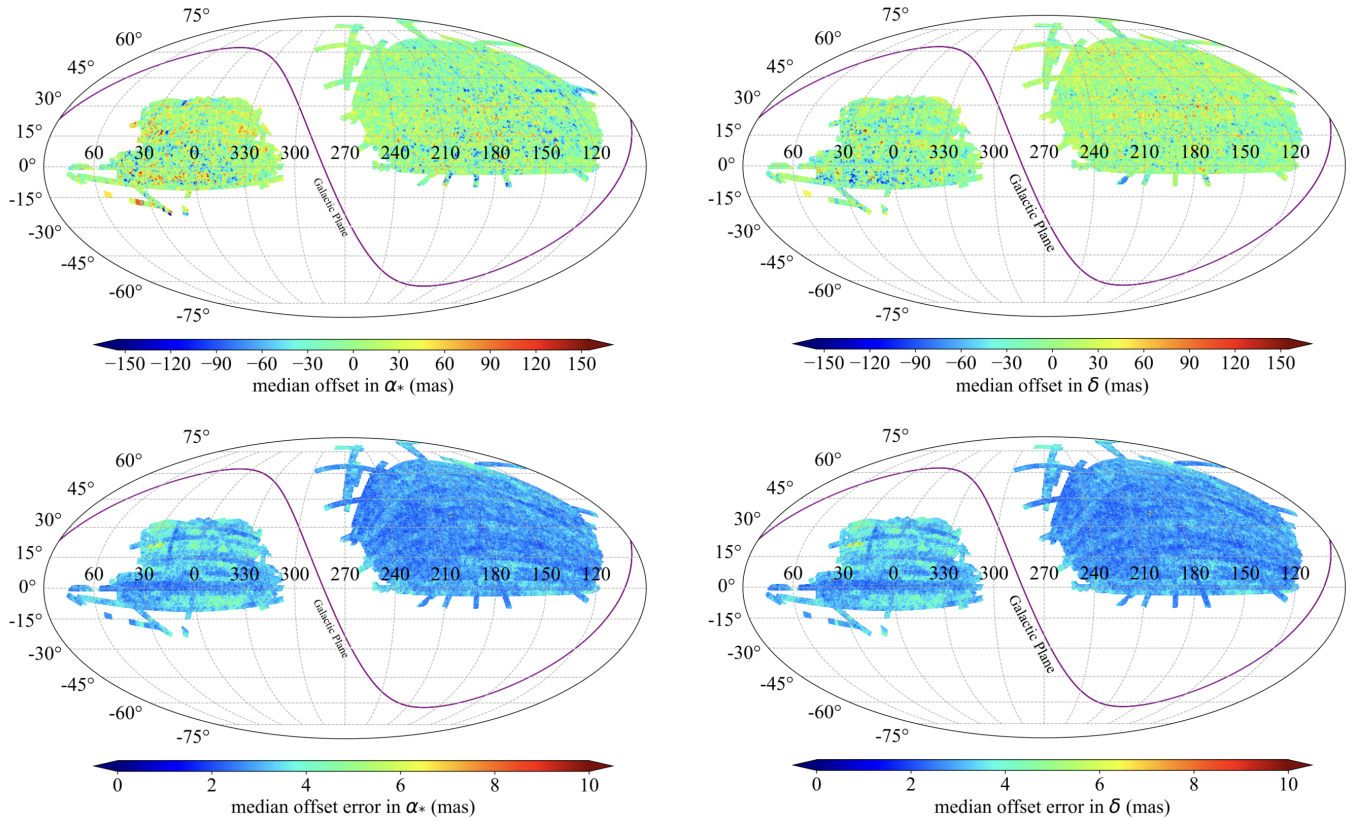


Figure 4: Spatial distribution of positional offsets (upper panels) and the offset errors (lower panels). The left and right panels represent the distributions for α_* and δ , respectively. The purple curves represent the Galactic plane.

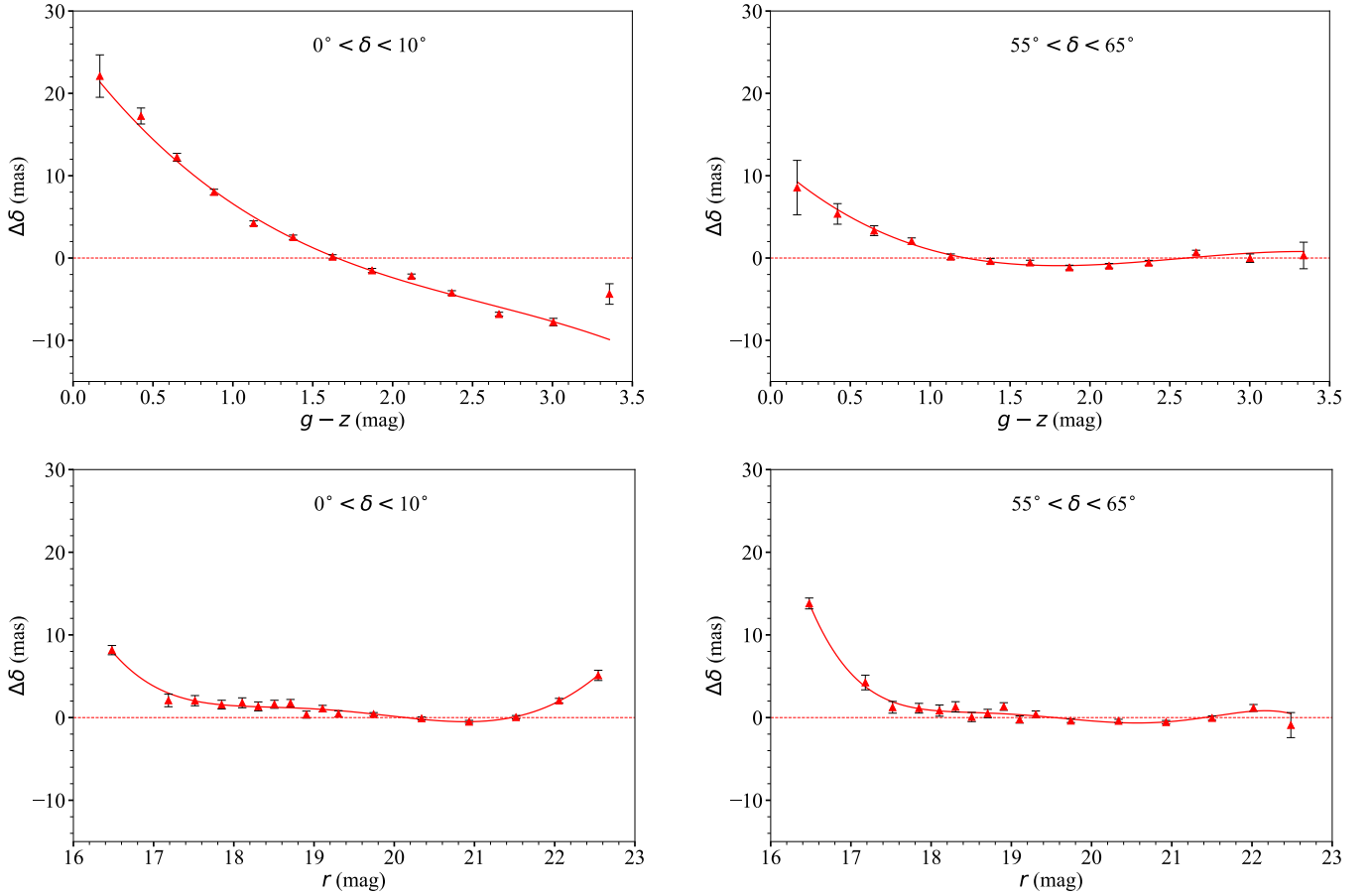


Figure 5: Positional offsets in δ vary with color and magnitude at different declinations. The top and bottom panels present the offsets as function of color and magnitude, respectively. The red triangles denote 3σ median positional discrepancies observed between the SDSS recorded galaxy positions and the established reference frame in different color/magnitude bins. The error bars are the corresponding standard deviation after 3σ -clipping, reflecting the dispersion of the data points around the median. The red curves are the best-fit polynomial.

vations (Δt):

$$\mu_{\alpha, \delta} = \frac{\alpha, \delta_{\text{DESI}} - \alpha, \delta_{\text{SDSS}}}{\Delta t}. \quad (1)$$

4. THE PRECISION ANALYSES

Various celestial objects, including galaxies, quasars, remote stars, and sources in other proper motion catalogs can be used to verify the precision of our derived proper motions. Galaxies and quasars, due to their immense distances, exhibit near-zero proper motion. Thus, the mean and standard deviation of their measured proper motions can directly quantify the systematic and random errors inherent in our measurements. Nevertheless, galaxies, being extended and potentially asymmetric entities, suffer from reduced positional measurement accuracy. Moreover, quasars with pronounced emission lines can present unique challenges related to DCR. Halo stars, though distant, still exhibit measurable proper motion that cannot be disregarded. Consequently, each validation methodology boasts its own merits and constraints, warranting individual examination and discussion.

4.1. Galaxies

The measured proper motions of galaxies with $16 < r < 21.5$ can be used to evaluate the systematic and random errors. Figure 6 shows the spatial distribution of the systematic and random errors. As depicted in this figure, the vast majority of systematic errors are confined beneath 1 mas yr^{-1} . It is noteworthy that galaxies, being extended objects, are prone to having larger positional uncertainties than point sources, consequently inflating the random errors associated with their inferred proper motions. Moreover, the data reveal a pattern in SGC with discernibly heightened random errors. This pattern perfectly aligns with the sequential observation scheme of the SDSS observing runs, as illustrated in Figure 2. We also compare the SDSS and Gaia data and confirm its existence. The shorter time span between observations is detrimental to the accuracy of proper motion measurements.

4.2. Quasars

Consistent with the galaxy analysis, we evaluate both systematic and random errors in proper motion utilizing a dataset comprising 734,012 spectroscopically verified quasars from the SDSS. We also find that the random errors in the SGC are significantly higher than those ($\sim 3 \text{ mas yr}^{-1}$) in the NGC. Given the high positional accuracy achievable with point-like quasars, the resultant random errors in their inferred proper motions are considerably diminished relative to those of galaxies.

The proper motion characteristics of quasars with $16 < r < 21.5$ conform well to Gaussian distributions, as illustrated in Figure 7. Consequently, they serve as a reliable basis for estimating the systematic and random errors present in our DESI-SDSS proper motion catalog. The median values of the proper motion components μ_{α^*} and μ_{δ} are estimated to be 0.15 mas yr^{-1} and 0.11 mas yr^{-1} , respectively. The standard deviation around these median values (random error) is measured at 3.65 mas yr^{-1} for α^* and 3.72 mas yr^{-1} for δ .

Beyond the distributions, we further analyze the precision of quasar proper motions with respect to their colors and magnitudes. Figure 8 shows the proper motions of quasars as functions of the $g-z$ color and the r -band magnitude. It can be seen that the systematic error exhibits only minimal variation with color. Conversely, redder quasars tend to exhibit more significant random error, a trend potentially skewed by an underrepresentation of quasar samples in the red-color range. Moreover, both systematic and random errors become more pronounced at fainter magnitudes. Specifically, systematic errors surpass 0.5 mas yr^{-1} at $r > 21$, while random errors escalate gradually with increasing magnitude, ranging from approximately 2.5 to 5 mas yr^{-1} for objects with $r < 21$. The random error can be as high as around 8 mas yr^{-1} at $r = 23$.

4.3. Distant Stars

We employ a total of 5,307 distant ($\geq 10 \text{ kpc}$) halo stars sourced from Zhang et al. (2023), to assess the precision of our proper motion determinations. Although their velocities relative to the Galactic center are small, the influence of solar motion must still be taken into account. Therefore, a correction for solar motion is implemented, assuming a solar velocity vector of $(U_{\odot}, V_{\odot}, W_{\odot}) = (11.1, 12.24, 7.25) \text{ km s}^{-1}$ (Schönrich et al. 2010), alongside a local standard of rest (LSR) circular velocity of $V_{\text{LSR}} = 220 \text{ km s}^{-1}$. The resultant corrected proper motions of these halo stars are shown in Figure 9. It shows the median values of $\mu_{\alpha^*} = -0.39 \text{ mas yr}^{-1}$ and $\mu_{\delta} = -0.25 \text{ mas yr}^{-1}$ with associated dispersions of 3.00 mas yr^{-1} and 2.95 mas yr^{-1} , respectively.

4.4. Comparison with proper motions from SDSS Stripe 82

Bramich et al. (2008) released a proper motion catalog containing nearly 4 million objects in the SDSS Stripe 82 (hereafter S82). We cross-match the stars in S82 with our catalog to verify the consistency of the proper motion determinations. Given the high galactic latitudes of DESI observations, the stars in S82 predominantly belong to the thick disk and halo components of the Milky Way. To target the thick disk population characterized by larger proper motions, we imposed a color criterion of $g - r > 1$, leading to the selection of 21,657 stars. Figure 10 illustrates the comparison of our proper motions of these chosen stars with those of S82. A remarkable correlation between the two sets of proper motion measurements can be seen from this figure, although there is a considerable dispersion. This scatter is largely attributed to the astrometric inaccuracies in S82 as reported in Bramich et al. (2008), particularly for sources fainter than $r=20$.

5. OUR PROPER MOTION CATALOG AND AN APPLICATION EXAMPLE

5.1. Our proper motion catalog and its limitations

Our DESI-SDSS proper motion catalog provides the proper motion measurements for 206.6 million non-Gaia objects. The catalog can be accessed at <https://www.scidb.cn/s/YzaIv2>. We also attempt to utilize the quasars to estimate the proper motion error. It is a function of the spatial posi-

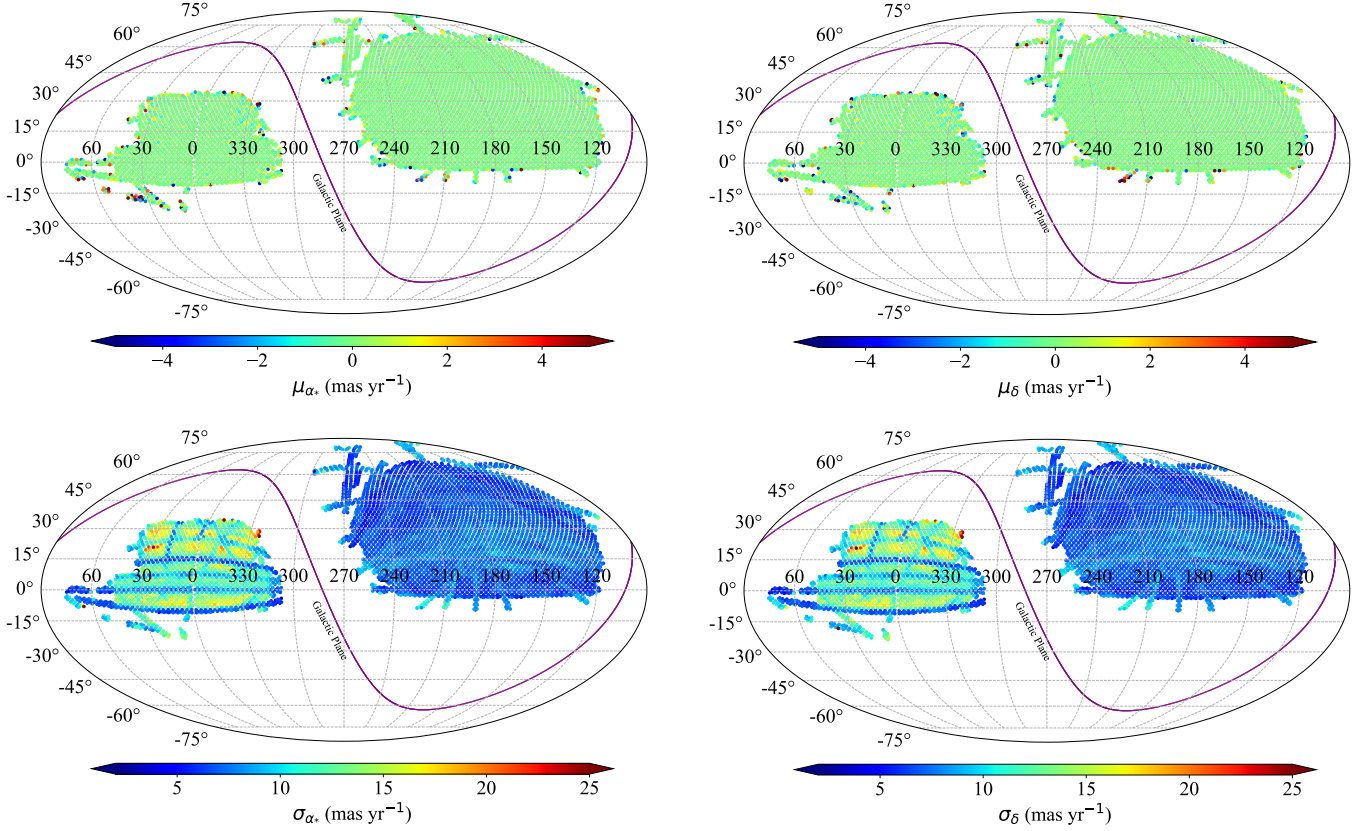


Figure 6: Spatial distribution of the systematic (top panels) and random errors (bottom panels) with respect to galaxies. The left and right panels show the errors for α_* and δ , respectively. The purple curves represent the Galactic plane.

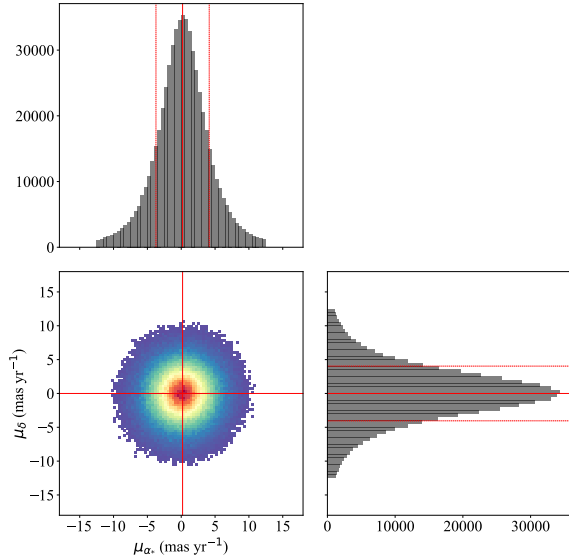


Figure 7: Distribution of proper motions for quasars. The top and right subplots present the histograms of μ_{α_*} and μ_{δ} , respectively. The red lines denotes the median and standard deviation values for both the α_* and δ components.

tion, color and magnitude:

$$\sigma_{\mu_{\alpha, \delta}} = f(\alpha, \delta, r, g - z), \quad (2)$$

where $f(\alpha, \delta, r, g - z)$ represents a series of two-dimensional polynomial models fitted to the proper motion errors, which account for variations with respect to magnitude and color. These models are developed for distinct spatial positions. Specifically, for a given pixel at (α_i, δ_j) , the corresponding function $f_{i,j}$ is derived through fitting against quasar samples situated within a 5° radius around that pixel.

Table 1 in Appendix B outlines the content of our catalog. In addition to proper motion and its error, it encompasses fundamental details extracted from both the SDSS and DESI databases, such as source positions, magnitudes, and object classifications. For enhanced user accessibility, we have incorporated the Gaia proper motion data as well, which come from the released data of DR2 ¹.

It should be noted that our proper motion catalog also has several limitations:

- Our analysis focused exclusively on the proper motion of objects not covered by Gaia, as the current DESI LS catalog lacks positional data for sources already detected by Gaia.
- The proper motion uncertainties, represented by PMRA_ERR and PMDEC_ERR, are provided as statis-

¹ <https://www.legacysurvey.org/dr10/description/#astrometry>

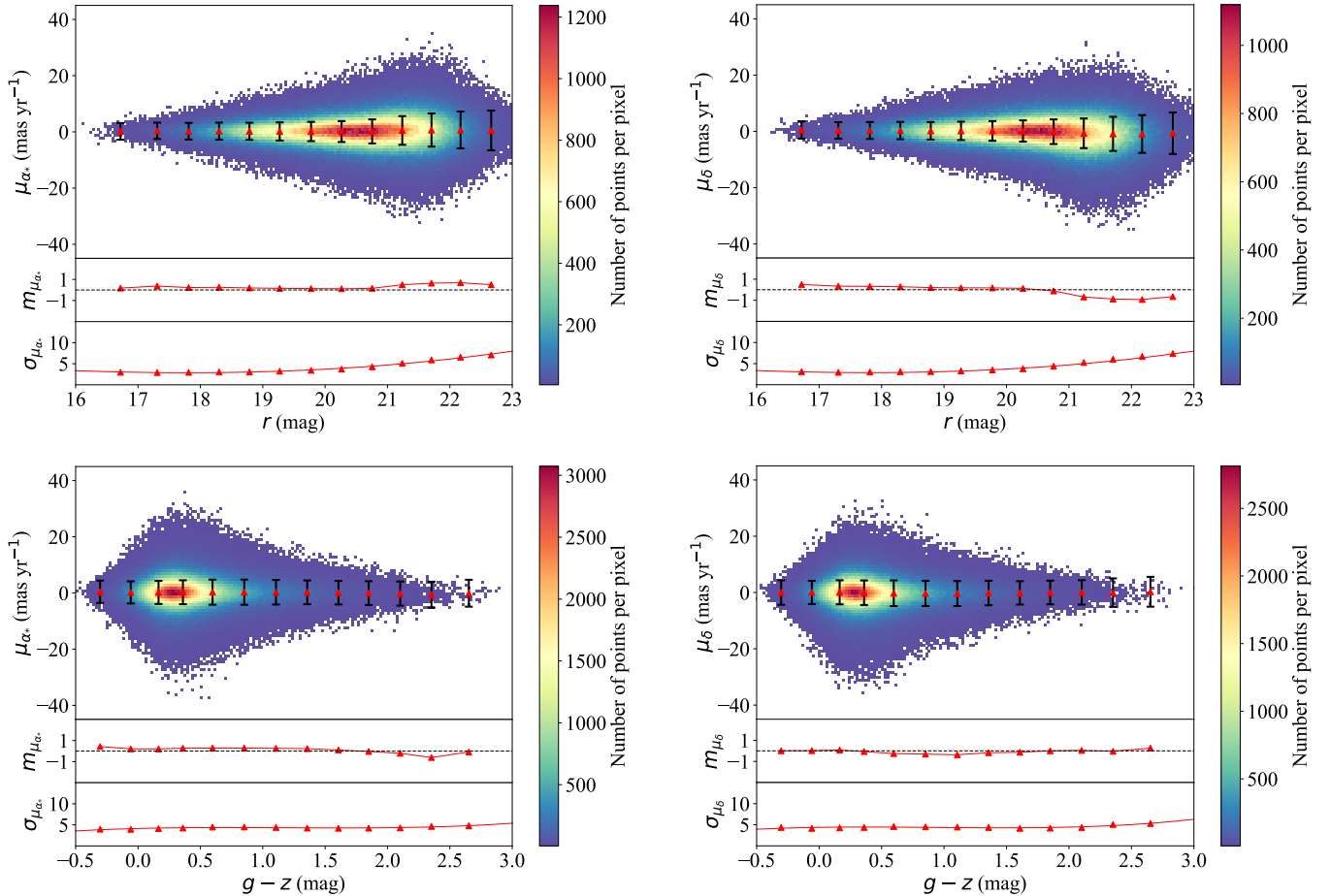


Figure 8: Proper motions of quasars as functions of color (left subplots) and magnitude (right subplots). The upper and lower subplots separately depict the α_* and δ components. Each subplot encompasses the full dataset of 734 k quasars. The red triangles with error bars represent the median and dispersion of each color or magnitude bin. The median and dispersion as function of color and magnitude are also plotted in the middle and lower panels.

tical estimates and do not reflect measurements derived from individual targets.

- The observation time interval of targets in SGC is shorter, which causes the proper motion measurement error to be 2–3 times larger than other areas.
- Targets observed in the SGC feature a shorter time interval between observations, leading to proper motion measurement errors that are two to three times greater compared to those in other regions.
- Employing galaxies from the DESI Legacy Survey as the reference frame is susceptible to distortive effects induced by DCR. This issue is further compounded by the reliance on co-added positional information from multiple exposures inherent to the current DESI catalog, thereby increasing the complexity of the analysis.
- Both SDSS and DESI supply morphological classifications for the objects as provided in our catalog. Users can incorporate additional information such as color to achieve a more refined physical classification.

5.2. Applying our catalog to estimate the proper motions of star clusters

Stars within a star cluster exhibit a collective motion, enabling us to leverage clusters with precisely known proper motions to validate our proper motion measurements and refine them using fainter cluster members. This study employs star clusters documented in the Milky Way Star Clusters Catalog (MWSC; Kharchenko et al. 2012, 2013; Schmeja et al. 2014; Scholz et al. 2015). Only 17 star clusters (15 globular and 2 open clusters) have sufficient number of members in the DESI-SDSS footprint.

For each cluster, we select cluster members as those stars within the cluster radius and located close to the theoretical isochrone on the color-magnitude diagram (CMD). The cluster radius and the stellar population parameters (e.g. age, metallicity and distance modulus) come from the MWSC catalog. Theoretical isochrones are obtained from CMD 3.7². The left panel of Figure 11 presents the CMD overlaid

² <http://stev.oapd.inaf.it/cgi-bin/cmd>

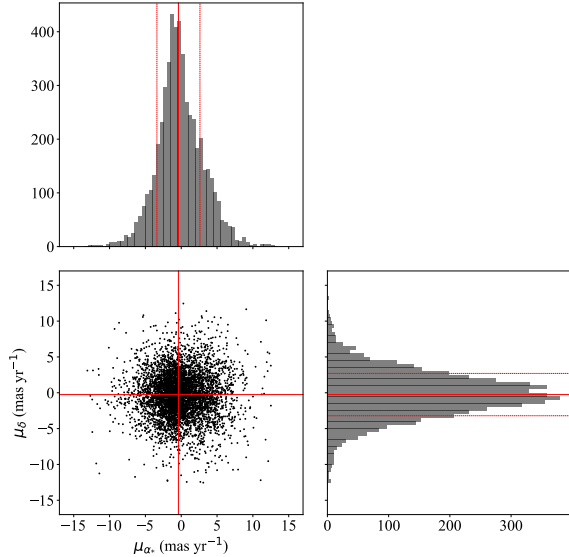


Figure 9: Corrected proper motion distribution of distant halo stars, with solar motion effects accounted for correcting for the solar motion. The top and right subplots present the histograms of μ_{α_*} and μ_{δ} , respectively. Red lines denote the median proper motion and corresponding standard deviations for α_* and δ .

with the theoretical isochrone for Palomar 5 as an example. Stars belonging to a cluster exhibit inherent scatter in their positioning along the isochrone on the CMD. Consequently, we identify potential cluster members as those stars situated within a radius of 0.14° of the cluster center, along with those that fall within a band encompassing 1σ photometric uncertainty augmented by an additional intrinsic dispersion of 0.05 mag around the isochrone path (dashed curves in Figure 11). The right panel of Figure 11 illustrates the proper motion distribution for the cluster members that are not part of the Gaia dataset. The mean proper motion of the cluster is estimated as $\mu_{\alpha_*} = -3.52 \text{ mas yr}^{-1}$ and $\mu_{\delta} = -4.08 \text{ mas yr}^{-1}$. The corresponding errors are 0.24 mas yr^{-1} for α_* and 0.22 mas yr^{-1} for δ . Similarly, the Gaia member stars and the cluster proper motion and its uncertainty based on these members are computed in the same manner.

Figure 12 presents a comparison of the proper motion for star clusters derived using our and Gaia catalogs. A robust linear correlation is evident between these two measurements. It highlights a congruent measurement of proper motion when employing bright stars available in Gaia or fainter stars detectable in DESI. Table 2 in Appendix B lists the basic information and proper motions for all 17 star clusters.

6. CONCLUSIONS

We have successfully established the DESI-SDSS proper motion catalog through the construction of a reference frame utilizing galaxies, with subsequent corrections for position-, color-, and magnitude-dependent astrometric discrepancies. Despite the relatively lower astrometric precision of ground-based surveys such as SDSS and DESI in contrast to space-

based counterparts, the extensive temporal baseline of about 13 years partly mitigates this deficiency. Our proper motion accuracy has been validated through multiple tests involving galaxies, quasars, remote stars, and cross-referencing with SDSS Stripe 82 data.

Based on an analysis of 734,012 quasars, the systematic errors in our proper motion measurements were quantified at 0.15 mas yr^{-1} in α_* and 0.11 mas yr^{-1} in δ , with random errors of 3.65 mas yr^{-1} and 3.72 mas yr^{-1} in α_* and δ , respectively. The proper motion of stars and galaxies reveals a systematic difference in the proper motion errors between NGC and SGC due to different time baselines. The distant halo stars give a precision better than 3.0 mas yr^{-1} . A comparative study with SDSS Stripe 82 using 21,657 stars confirms a favorable agreement, reinforcing the reliability of our catalog.

As a practical demonstration, we applied our catalog to calculate the proper motions for 17 star clusters. The agreement between the proper motions derived from Gaia and those from our DESI-SDSS catalog demonstrates a strong consistency. Thus, our DESI-SDSS proper motion catalog stands as a valuable resource, effectively bridging the sensitivity gap left by Gaia at the faint magnitude end. Coupled with extensive DESI imaging data, this catalog can facilitate the detection of substructures within the Galactic halo, thereby advancing our insights into its origin and composition.

ACKNOWLEDGMENTS

The authors acknowledge the supports from the Beijing Municipal Natural Science Foundation (grant No. 1222028), the National Key R&D Program of China (grant Nos. 2022YFA1602902, 2023YFA1607800, 2023YFA1607804, 2023YFA1608100, and 2023YFF0714800), and the National Natural Science Foundation of China (NSFC; grant Nos. 12120101003, 12373010, 12173051, and 12233008). The authors also acknowledge the science research grants from the China Manned Space Project with Nos. CMS-CSST-2021-A02 and CMS-CSST-2021-A04 and the Strategic Priority Research Program of the Chinese Academy of Sciences with Grant Nos. XDB0550100 and XDB0550000.

The DESI Legacy Imaging Surveys consist of three individual and complementary projects: the Dark Energy Camera Legacy Survey (DECaLS), the Beijing-Arizona Sky Survey (BASS), and the Mayall z-band Legacy Survey (MzLS). DECaLS, BASS and MzLS together include data obtained, respectively, at the Blanco telescope, Cerro Tololo Inter-American Observatory, NSF’s NOIRLab; the Bok telescope, Steward Observatory, University of Arizona; and the Mayall telescope, Kitt Peak National Observatory, NOIRLab. NOIRLab is operated by the Association of Universities for Research in Astronomy (AURA) under a cooperative agreement with the National Science Foundation. Pipeline processing and analyses of the data were supported by NOIRLab and the Lawrence Berkeley National Laboratory (LBNL). Legacy Surveys also uses data products from the Near-Earth Object Wide-field Infrared Survey Explorer (NEOWISE),

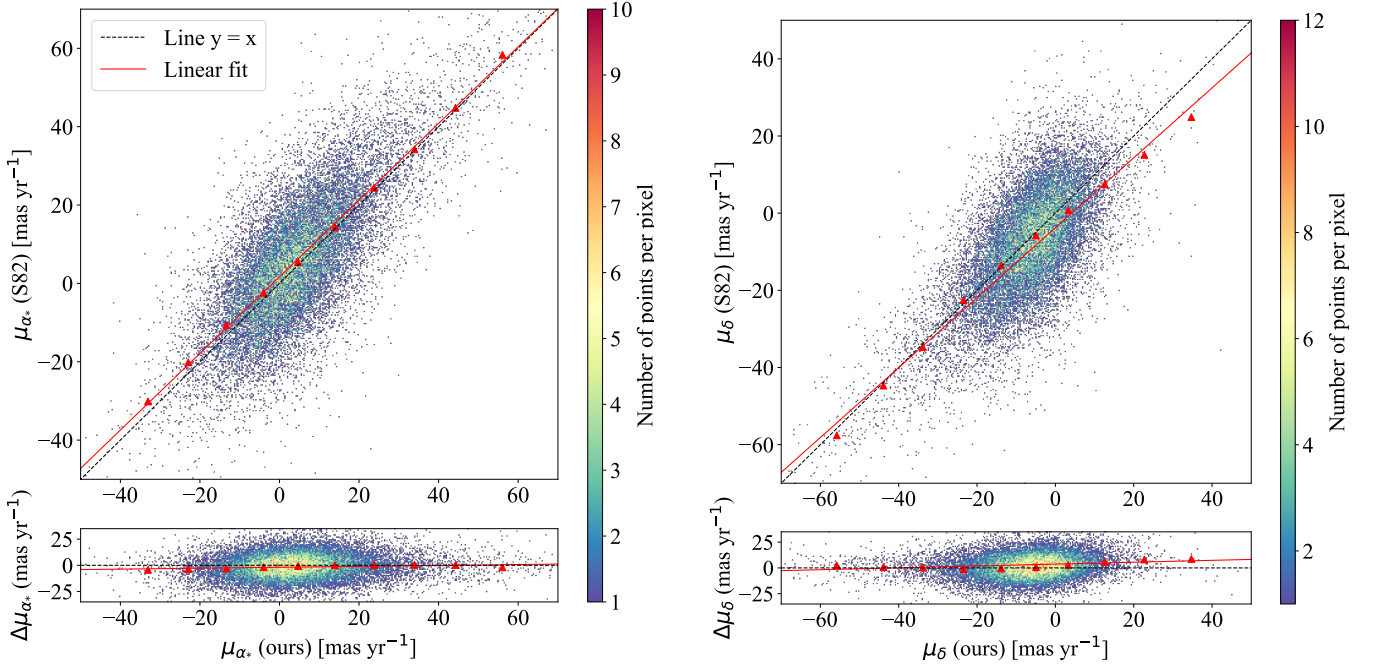


Figure 10: Comparison of our proper motions with those from SDSS S82 for μ_{α_*} (left) and μ_{δ} (right). Red solid lines present the linear relationship of our and S82 measurements, and the black dashed lines in top and bottom panels mark $y = x$ and $y = 0$, respectively.

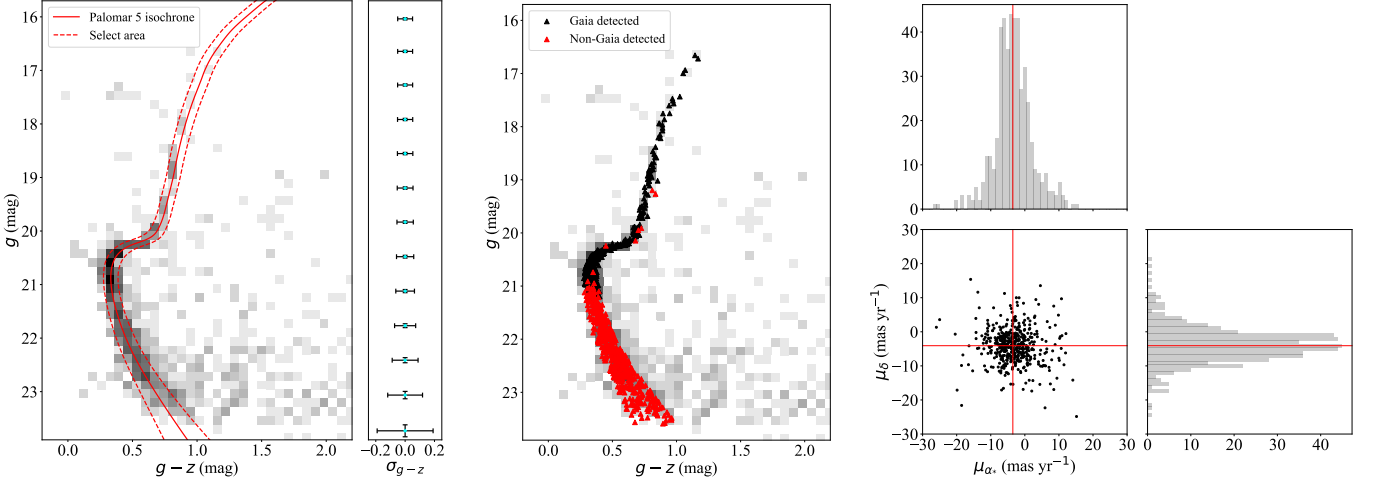


Figure 11: Left: color-magnitude diagram for Palomar 5, featuring all stars within the cluster radius of 0.14° . The solid red curve delineates the theoretical isochrone, while the dashed red envelopes enclosing it symbolize a combined 1σ photometric uncertainty coupled with an intrinsic color error of 0.05 mag. To the right of the CMD, cyan dots accompanied by error bars illustrate the magnitude and color measurement uncertainties. The region enclosed by the dashed lines is used to select member stars. Middle: selected Gaia (black triangles) and non-Gaia (red triangles) member stars within the CMD. Right: proper motion distribution of non-Gaia member stars. The median values for α_* and δ are marked with solid red lines. The top and right subplots present the distributions of μ_{α_*} and μ_{δ} , respectively.

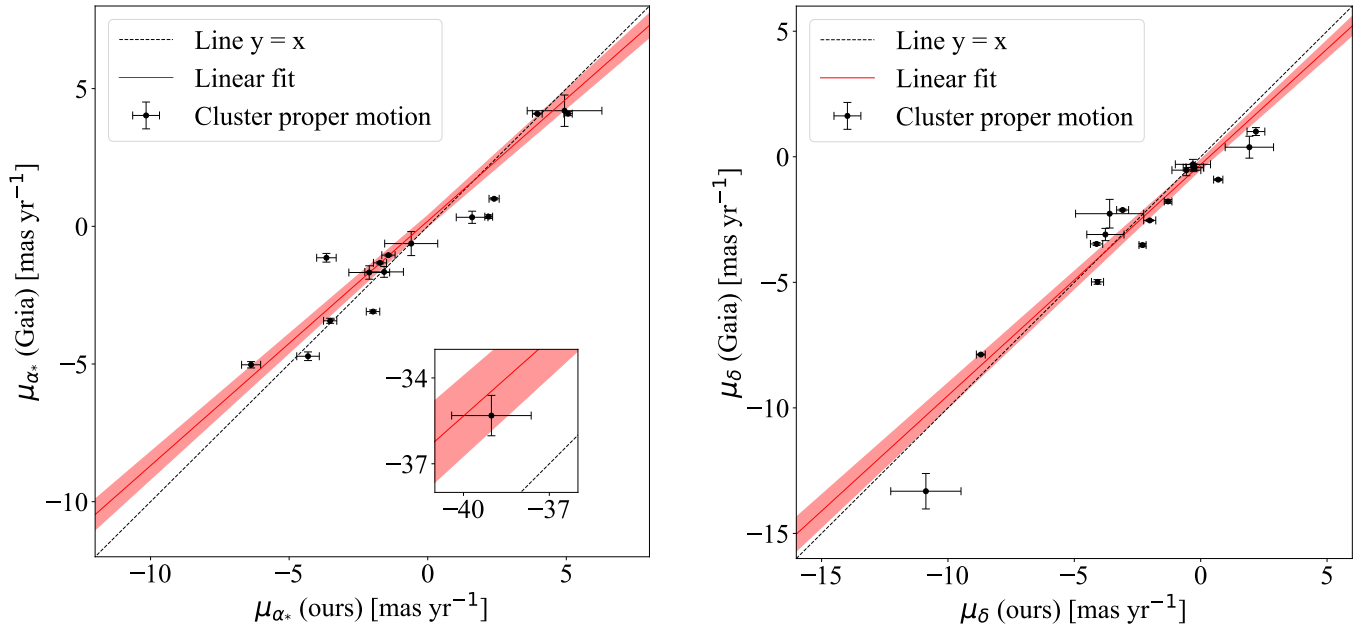


Figure 12: Comparison of proper motions for 17 star clusters derived from both our and Gaia catalogs. The left panel focuses on the comparison of μ_{α^*} , with a dedicated inset (bottom right) highlighting NGC 2632 due to its notably high proper motion, facilitating clearer visualization. The right panel presents the corresponding comparison for μ_{δ} . In each panel, red shaded regions envelop the linear regression fits, representing the estimated uncertainty bounds associated with the linear relationship between our measurements and those from the Gaia catalog. The black dashed line displays $y = x$.

a project of the Jet Propulsion Laboratory/California Institute of Technology, funded by the National Aeronautics and Space Administration. Legacy Surveys was supported by: the Director, Office of Science, Office of High Energy Physics of the U.S. Department of Energy; the National Energy Research Scientific Computing Center, a DOE Office of Science User Facility; the U.S. National Science Foundation, Division of Astronomical Sciences; the National Astronomical Observatories of China, the Chinese Academy of Sciences and the Chinese National Natural Science Foundation. LBNL is managed by the Regents of the University of California under contract to the U.S. Department of Energy. The complete acknowledgments can be found at <https://www.legacysurvey.org/acknowledgment/>.

Funding for SDSS-III has been provided by the Alfred P. Sloan Foundation, the Participating Institutions, the National Science Foundation, and the U.S. Department of Energy Office of Science. The SDSS-III web site is <http://www.sdss3.org/>. SDSS-III is managed by the Astrophysical Research Consortium for the Participating Institutions of the SDSS-III Collaboration including the University of

Arizona, the Brazilian Participation Group, Brookhaven National Laboratory, Carnegie Mellon University, University of Florida, the French Participation Group, the German Participation Group, Harvard University, the Instituto de Astrofísica de Canarias, the Michigan State/Notre Dame/JINA Participation Group, Johns Hopkins University, Lawrence Berkeley National Laboratory, Max Planck Institute for Astrophysics, Max Planck Institute for Extraterrestrial Physics, New Mexico State University, New York University, Ohio State University, Pennsylvania State University, University of Portsmouth, Princeton University, the Spanish Participation Group, University of Tokyo, University of Utah, Vanderbilt University, University of Virginia, University of Washington, and Yale University.

This work presents results from the European Space Agency (ESA) space mission Gaia. Gaia data are being processed by the Gaia Data Processing and Analysis Consortium (DPAC). Funding for the DPAC is provided by national institutions, in particular the institutions participating in the Gaia MultiLateral Agreement (MLA). The Gaia mission website is <https://www.cosmos.esa.int/gaia>. The Gaia archive website is <https://archives.esac.esa.int/gaia>.

REFERENCES

- Abazajian, K. N., Adelman-McCarthy, J. K., Agüeros, M. A., et al. 2009, *The Astrophysical Journal Supplement Series*, 182, 543
- Aihara, H., Prieto, C. A., An, D., et al. 2011, *The Astrophysical Journal Supplement Series*, 193, 29
- Blum, R. D., Burleigh, K., Dey, A., et al. 2016, in *American Astronomical Society Meeting Abstracts*, Vol. 228, American Astronomical Society Meeting Abstracts #228, 317.01
- Bramich, D., Vidrih, S., Wyrzykowski, L., et al. 2008, *Monthly Notices of the Royal Astronomical Society*, 386, 887
- Cantat-Gaudin, T. 2022, *Universe*, 8, 111
- Chambers, K. C., Magnier, E., Metcalfe, N., et al. 2016, arXiv preprint arXiv:1612.05560
- Cooper, A. P., Kposov, S. E., Prieto, C. A., et al. 2023, *The Astrophysical Journal*, 947, 37
- Dark Energy Survey Collaboration, Abbott, T., Abdalla, F. B., et al. 2016, *MNRAS*, 460, 1270, doi: [10.1093/mnras/stw641](https://doi.org/10.1093/mnras/stw641)
- DESI Collaboration, Aghamousa, A., Aguilar, J., et al. 2016, arXiv e-prints, arXiv:1611.00036, doi: [10.48550/arXiv.1611.00036](https://doi.org/10.48550/arXiv.1611.00036)
- Dey, A., Schlegel, D. J., Lang, D., et al. 2019, *AJ*, 157, 168, doi: [10.3847/1538-3881/ab089d](https://doi.org/10.3847/1538-3881/ab089d)
- Drimmel, R., Romero-Gómez, M., Chemin, L., et al. 2023, *Astronomy & Astrophysics*, 674, A37
- Fedorov, P. N., Myznikov, A. A., & Akhmetov, V. S. 2009, *MNRAS*, 393, 133, doi: [10.1111/j.1365-2966.2008.14168.x](https://doi.org/10.1111/j.1365-2966.2008.14168.x)
- Fritz, T., Gillessen, S., Trippe, S., et al. 2010, *Monthly Notices of the Royal Astronomical Society*, 401, 1177, doi: [10.1111/j.1365-2966.2009.15707.x](https://doi.org/10.1111/j.1365-2966.2009.15707.x)
- Fukugita, M., Shimasaku, K., Ichikawa, T., Gunn, J., et al. 1996, *The Sloan digital sky survey photometric system*, Tech. rep., SCAN-9601313
- Gaia Collaboration, Brown, A. G. A., Vallenari, A., et al. 2016, *A&A*, 595, A2, doi: [10.1051/0004-6361/201629512](https://doi.org/10.1051/0004-6361/201629512)
- . 2018, *A&A*, 616, A1, doi: [10.1051/0004-6361/201833051](https://doi.org/10.1051/0004-6361/201833051)
- Gaia Collaboration, Vallenari, A., Brown, A. G. A., et al. 2023, *A&A*, 674, A1, doi: [10.1051/0004-6361/202243940](https://doi.org/10.1051/0004-6361/202243940)
- Gorski, K. M., Hivon, E., Banday, A. J., et al. 2005, *The Astrophysical Journal*, 622, 759
- Gunn, J. E., Carr, M., Rockosi, C., et al. 1998, *AJ*, 116, 3040, doi: [10.1086/300645](https://doi.org/10.1086/300645)
- Gunn, J. E., Siegmund, W. A., Mannery, E. J., et al. 2006, *AJ*, 131, 2332, doi: [10.1086/500975](https://doi.org/10.1086/500975)
- Hambly, N., Davenhall, A., Irwin, M., & MacGillivray, H. 2001, *Monthly Notices of the Royal Astronomical Society*, 326, 1315
- Helmi, A. 2020, *Annual Review of Astronomy and Astrophysics*, 58, 205, doi: <https://doi.org/10.1146/annurev-astro-032620-021917>
- Hog, E., Fabricius, C., Makarov, V., et al. 2000, *Astronomy and Astrophysics*, 363, 385
- Hogg, D. W., Finkbeiner, D. P., Schlegel, D. J., & Gunn, J. E. 2001, *The Astronomical Journal*, 122, 2129
- Kaczmarczik, M. C., Richards, G. T., Mehta, S. S., & Schlegel, D. J. 2009, *AJ*, 138, 19, doi: [10.1088/0004-6256/138/1/19](https://doi.org/10.1088/0004-6256/138/1/19)
- Katz, D., Antoja, T., Romero-Gómez, M., et al. 2018, *Astronomy & Astrophysics*, 616, A11

- Kharchenko, N. V., Piskunov, A. E., Schilbach, E., Röser, S., & Scholz, R. D. 2012, *A&A*, 543, A156, doi: [10.1051/0004-6361/201118708](https://doi.org/10.1051/0004-6361/201118708)
- . 2013, *A&A*, 558, A53, doi: [10.1051/0004-6361/201322302](https://doi.org/10.1051/0004-6361/201322302)
- Lindgren, L., Lammers, U., Bastian, U., et al. 2016, *Astronomy & Astrophysics*, 595, A4
- Malhan, K., Ibata, R. A., & Martin, N. F. 2018, *Monthly Notices of the Royal Astronomical Society*, 481, 3442
- Monet, D. G., Levine, S. E., Canzian, B., et al. 2003, *The Astronomical Journal*, 125, 984, doi: [10.1086/345888](https://doi.org/10.1086/345888)
- Munn, J. A., Monet, D. G., Levine, S. E., et al. 2004, *AJ*, 127, 3034, doi: [10.1086/383292](https://doi.org/10.1086/383292)
- Peng, X., Qi, Z., Wu, Z., et al. 2015, *PASP*, 127, 250, doi: [10.1086/680447](https://doi.org/10.1086/680447)
- Qi, Z., Yu, Y., Bucciarelli, B., et al. 2015, *AJ*, 150, 137, doi: [10.1088/0004-6256/150/4/137](https://doi.org/10.1088/0004-6256/150/4/137)
- Qiu, T., Wang, W., Takada, M., et al. 2021, *MNRAS*, 501, 5149, doi: [10.1093/mnras/staa3975](https://doi.org/10.1093/mnras/staa3975)
- Roeser, S., Demleitner, M., & Schilbach, E. 2010, *AJ*, 139, 2440, doi: [10.1088/0004-6256/139/6/2440](https://doi.org/10.1088/0004-6256/139/6/2440)
- Schlegel, D. J., Finkbeiner, D. P., & Davis, M. 1998, *The Astrophysical Journal*, 500, 525
- Schmeja, S., Kharchenko, N. V., Piskunov, A. E., et al. 2014, *A&A*, 568, A51, doi: [10.1051/0004-6361/201322720](https://doi.org/10.1051/0004-6361/201322720)
- Scholz, R. D., Kharchenko, N. V., Piskunov, A. E., Röser, S., & Schilbach, E. 2015, *A&A*, 581, A39, doi: [10.1051/0004-6361/201526312](https://doi.org/10.1051/0004-6361/201526312)
- Schönrich, R., Binney, J., & Dehnen, W. 2010, *MNRAS*, 403, 1829, doi: [10.1111/j.1365-2966.2010.16253.x](https://doi.org/10.1111/j.1365-2966.2010.16253.x)
- Silva, D. R., Blum, R. D., Allen, L., et al. 2016, in *American Astronomical Society Meeting Abstracts*, Vol. 228, *American Astronomical Society Meeting Abstracts #228*, 317.02
- Skrutskie, M. F., Cutri, R. M., Stiening, R., et al. 2006, *AJ*, 131, 1163, doi: [10.1086/498708](https://doi.org/10.1086/498708)
- Stoughton, C., Lupton, R. H., Bernardi, M., et al. 2002, *AJ*, 123, 485, doi: [10.1086/324741](https://doi.org/10.1086/324741)
- Tian, H.-J., Gupta, P., Sesar, B., et al. 2017, *ApJS*, 232, 4, doi: [10.3847/1538-4365/aa826a](https://doi.org/10.3847/1538-4365/aa826a)
- York, D. G., Adelman, J., Anderson Jr, J. E., et al. 2000, *The Astronomical Journal*, 120, 1579
- Zacharias, N., Finch, C. T., Girard, T. M., et al. 2013, *AJ*, 145, 44, doi: [10.1088/0004-6256/145/2/44](https://doi.org/10.1088/0004-6256/145/2/44)
- Zacharias, N., Urban, S. E., Zacharias, M. I., et al. 2000, *The Astronomical Journal*, 120, 2131, doi: [10.1086/301563](https://doi.org/10.1086/301563)
- Zhang, L., Xue, X.-X., Yang, C., et al. 2023, *AJ*, 165, 224, doi: [10.3847/1538-3881/acc9bb](https://doi.org/10.3847/1538-3881/acc9bb)
- Zou, H., Zhou, X., Jiang, Z., et al. 2016, *AJ*, 151, 37, doi: [10.3847/0004-6256/151/2/37](https://doi.org/10.3847/0004-6256/151/2/37)
- Zou, H., Zhou, X., Fan, X., et al. 2017, *PASP*, 129, 064101, doi: [10.1088/1538-3873/aa65ba](https://doi.org/10.1088/1538-3873/aa65ba)

APPENDIX

A. OUR PROPER MOTION CATALOG

Table 1 summarizes the basic information of our proper motion catalog. It comprises photometric parameters originating from the DESI and SDSS photometric datasets, such as celestial coordinates, magnitudes, and morphological classifications. The catalog provides the proper motions and corresponding errors for objects not included in Gaia, which are derived from our comparative analysis between the SDSS and DESI astrometric measurements. It also contains Gaia objects, whose proper motions are inherited from the Gaia DR2.

Table 1: Our proper motion catalog.

Column	Unit	Format	Description
objID		Long	SDSS unique object identifier
ID		Long	Object ID in DESI
RA	degree	Double	Right ascension in J2000 from DESI
RA_IVAR	1/degree ²	Float	Inverse variance of RA
DEC	degree	Double	Declination in J2000 from DESI
DEC_IVAR	1/degree ²	Float	Inverse variance of DEC
PM_SOURCE		String	Source of proper motion (Gaia or DESI)
PMRA	mas yr ⁻¹	Double	Proper motion for α
PMDEC	mas yr ⁻¹	Double	Proper motion for δ
PMRA_ERR	mas yr ⁻¹	Double	proper motion error for α
PMDEC_ERR	mas yr ⁻¹	Double	proper motion error for δ
MJD_SDSS	days	Integer	Julian date of the SDSS observation
MJD_DESI	days	Double	mean Julian date of the DESI observations
TIME	year	Double	Time interval between SDSS and DESI observation
TYPE_SDSS		Short	Type of object (3=galaxy, 6=star) classified by SDSS
TYPE_DESI ^a		String	Type of object classified by DESI
MAG_G	mag	Float	DESI g -band magnitude
MAG_R	mag	Float	DESI r -band magnitude
MAG_Z	mag	Float	DESI z -band magnitude
MAGERR_G	mag	Float	DESI g -band magnitude error
MAGERR_R	mag	Float	DESI r -band magnitude error
MAGERR_Z	mag	Float	DESI z -band magnitude error

^a See more details at <https://www.legacysurvey.org/dr10/description/#morphological-classification>.

B. PROPER MOTIONS FOR 17 STAR CLUSTERS

Table 2 lists the proper motions estimated with both our catalog and the Gaia data.

Table 2: Proper motion and other parameters for 17 star clusters used in this work

NAME (1)	RA (2)	DEC (3)	EBV (4)	R (5)	D (6)	[Fe/H] (7)	AGE (8)	$\mu_{\alpha_e}^a$	μ_{δ}^a	$\sigma_{\mu_{\alpha_e}^a}$	$\sigma_{\mu_{\delta}^a}$	num ^a	$\mu_{\alpha_e}^b$	μ_{δ}^b	$\sigma_{\mu_{\alpha_e}^b}$	$\sigma_{\mu_{\delta}^b}$	num ^b
Koposov 2	119.571	26.25	0.021	0.07	16.725	-2.155	10.1	-0.596	1.926	0.957	1.45	43	-0.627	0.381	0.436	0.306	15
NGC 2419	114.535	38.882	0.083	0.12	19.61	-2.05	10.1	1.601	-0.566	0.572	0.795	96	0.328	-0.533	0.221	0.262	121
NGC 2420	114.596	21.567	0.01	0.305	12.3	-0.38	9.365	-1.722	-3.089	0.237	0.232	901.0	-1.327	-2.12	0.037	0.031	708
NGC 2632	130.095	19.69	0.01	3.1	6.363	0.094	8.92	-39.024	-10.873	1.39	1.317	116	-35.315	-13.319	0.706	0.395	804
NGC 4147	182.526	18.543	0.021	0.06	16.435	-1.645	10.1	-2.11	-3.77	0.736	0.725	174	-1.677	-3.096	0.244	0.18	142
NGC 5024	198.23	18.168	0.021	0.25	16.27	-1.75	10.1	2.395	0.694	0.183	0.193	1546	1.0	-0.91	0.038	0.038	1161
NGC 5053	199.113	17.7	0.01	0.15	16.206	-2.15	10.1	-3.655	2.186	0.352	0.321	543	-1.142	1.004	0.158	0.145	328
NGC 5272	205.548	28.377	0.01	0.44	15.045	-1.345	10.1	-1.418	-2.016	0.239	0.267	1506	-1.047	-2.535	0.036	0.045	2617
NGC 5466	211.38	28.534	0.0	0.205	16.021	-1.745	10.1	-6.372	-0.238	0.344	0.339	751	-5.028	-0.422	0.115	0.094	739
NGC 5904	229.638	2.081	0.029	0.44	14.385	-1.145	10.1	3.953	-8.7	0.176	0.178	1900	4.089	-7.876	0.02	0.019	3593
NGC 6205	250.422	36.46	0.021	0.47	14.265	-1.445	10.1	-1.974	-4.119	0.243	0.247	1403	-3.096	-3.471	0.059	0.062	1807
NGC 6229	251.745	47.528	0.01	0.165	17.425	-1.145	10.1	-1.573	-0.307	0.696	0.547	148	-1.655	-0.301	0.197	0.328	44
NGC 6341	259.281	43.136	0.021	0.405	14.6	-2.05	10.1	-4.319	-0.284	0.407	0.421	880	-4.718	-0.435	0.157	0.132	1192
NGC 7006	315.372	16.187	0.052	0.125	18.09	-1.52	10.1	4.936	-3.602	1.348	0.9	25	4.198	-2.267	0.57	0.621	43
NGC 7078	322.493	12.167	0.104	0.35	15.117	-2.05	10.1	2.2	-2.301	0.141	0.142	1468	0.351	-3.516	0.066	0.051	1428
NGC 7089	323.363	-0.823	0.062	0.26	15.325	-1.545	10.1	5.063	-1.29	0.152	0.154	1382	4.09	-1.779	0.073	0.063	1026
Palomar 5	229.022	-0.112	0.031	0.14	16.837	-1.245	10.1	-3.520	-4.082	0.239	0.218	477	-3.431	-4.984	0.092	0.072	419

Note. (1) Star cluster name. (2) R.A. in degrees (J2000). (3) Decl. in degrees (J2000). (4) Galactic reddening $E(B - V)$ in mag. (5) Angular radius of the cluster in degrees from MWSC. (6) Distance modulus of the cluster in mag. (7) Metallicity of the cluster. (8) Logarithm of the average age of the stars in the cluster in years.

^a Proper motion (in mas yr⁻¹) and the number of member stars derived from our catalog.

^b Proper motion and the number of member stars derived from the Gaia catalog.